



# Ion Implantation of Optical Ferroelectrics

CH. BUCHAL

*Institute for Thin Film and Ion Technology (ISI-IT), Forschungszentrum Juelich GmbH, D-52425 Juelich, Germany*

D. FLUCK & P. GÜNTER

*Institute of Quantum Electronics, ETH Hoenggerberg, 8093 Zuerich, Switzerland*

**Abstract.** We discuss ion implantation as a powerful non-equilibrium processing technology and show its potential for optical waveguide formation by damage engineering and by direct doping. Also the strong improvement of photorefractive properties by implantation-induced vacancies is demonstrated. Finally recent results of the growth of thin ferroelectric films by laser epitaxy and metal-organic vapor-phase epitaxy are presented. The combination of thin film growth techniques of optical ferroelectrics together with ion beam modification will prove important in this strongly advancing field.

**Keywords:** ion implantation, optical ferroelectrics, thin films

## 1. Introduction

Ion implantation is a well established standard process in the semiconductor industry [1]. It is used for local electrical doping and for local isolation. For example, an electronic silicon CMOS device chip receives between 10 and 20 different implantation steps. Another widespread application is the implantation treatment of metallic surfaces, where it very successfully improves surface hardness, corrosion resistance and wear. In this article we will discuss the application of ion implantation for the doping of optical ferroelectrics and especially the specific implantation generated lattice defects. Surprisingly, these defects modify the crystalline properties in a very useful way and “defect engineering” has become a technological approach. Primarily, these defects reduce the high atomic correlation in the optical ferroelectrics, thereby reducing the optical index. In addition, it has been shown, that the introduction of vacancies is equivalent to an electronic doping, thereby changing the majority carriers of photorefractive ferroelectric  $\text{KNbO}_3$  from holes to electrons.

Ion implantation is probably the most extreme non-equilibrium processing technique available for

research and production. The energy of the individual implanted ions is well controlled and in the range of several keV to MeV. When ions are impinging onto a solid, their kinetic energy is converted to heat, causing a local thermal spike. The corresponding energy density exceeds the values available during thermal treatments by many orders of magnitude. Nevertheless, thermalization of the individually deposited energy is quite rapid, typically on the picosecond time scale. This results in ultrarapid microscopic quenching with rates exceeding millions of K per second. On the same token, ion implantation is not restricted to the thermodynamic stability limits. For example, the implantation dose of any ion may exceed the equilibrium solubility of this ion in the target by large factors. Moreover, implantation is very versatile, because essentially any ion can be implanted into any target. The entire process is well controlled: the amount of implanted material is accurately determined from the charge collection, the depth of the ions is determined by the preset energy and the lateral extension of the implanted area can be defined by lithographical masks. Multiple energy implants and successive implantations of different ions permit the realization of complex

doping profiles and the implantation into heated targets offers unique combinations between thermally activated solid state reactions and the collision cascades, which are powered by the kinetic energy via momentum transfer.

The implantation of Co into Si leads to super-saturated phases. One observes the nucleation and growth of silicide precipitates or even planar solid state silicide epitaxy inside Si [2]. Silicide formation by ion implantation will become a valuable new process for special applications in the semiconductor device development.

Many metallic or semiconducting elements (or compounds) have been implanted into oxide substrates as  $\text{SiO}_2$  or  $\text{Al}_2\text{O}_3$  in order to form nanoparticles of very different optical properties inside the glassy or crystalline host [3]. To our knowledge, so far no such experiments have been performed with ferroelectric hosts or with ferroelectric nanoparticles.

## 2. Formation of Optical Waveguides in Highly Correlated Optical Ferroelectrics by Ion Implantation

### 2.1. Microscopic Mechanisms

The production of high quality optical waveguides in some of the optical oxide ferroelectrics is an extremely difficult task, because of structural phase transitions at low temperatures and the lack of efficient diffusion in the densely packed crystalline lattice. Only the ilmenite structure of  $\text{LiNbO}_3$  is exceptional: it permits waveguide formation by different diffusion schemes.

In the following, we will discuss the ion implantation into  $\text{KNbO}_3$ , because this ferroelectric material has been investigated very thoroughly. For a discussion of many other crystals the reader is referred to the monograph by Townsend [4] and the older book edited by Arnold and Mazzoldi [5].

A better understanding of the implantation effects follows from the details of the energy deposition in the target material. There are two main processes to be considered: a) scattering of the ions with electrons in the target and b) collisions with the nuclei, whereby part of the kinetic energy is transferred to the target nuclei. This causes atomic displacements. The rate of energy transfer for each process is a function of the nuclear charge and the mass of the incoming ion and

of the target. It also depends strongly on the energy. For light ions such as  $\text{H}^+$  and  $\text{He}^+$  and an energy in the range of 1 to 4 MeV, the two main processes are *electronic ionization* and *elastic nuclear collisions*, whereas inelastic nuclear collisions and elastic scattering from electrons are of minor importance for slowing down the incident ions.

Ion range and damage distribution predictions are essential for ion implantation and a variety of computer simulation programs have been developed. An inherent problem is that the generation of a realistic simulation of all events, that occur as an energetic ion travels through a target, requires a detailed knowledge of the types of interaction between the ion and target electrons and atoms. Ideally, the simulation should take account of the simultaneous motion of all the displaced atoms as well as the incoming ion and follow their motion until the material relaxes to thermal energies. To include all these possibilities is beyond the present understanding of the implantation processes as well as the available computational power.

One of the most widely used programs for modelling is TRIM (Transport of Ions in Matter) [6]. TRIM follows a large number of individual ion trajectories in the target. Each ion is then followed along through a sequence of collisions with the target atoms, making the assumption of straight free flight paths between collisions. The ion energy is reduced for each free-flight path by the electronic loss, and then—at a nuclear collision—by the nuclear energy loss, which is the result of momentum transfer to the target atom. It has been shown that the TRIM calculations are consistent with the experimental results in most cases.

At high velocity (ion energy  $> 10$  keV), the dominant energy loss for the  $\text{He}^+$  ions stems from electronic ionization that—to a first approximation—does not alter the refractive index, although 99.8% of the total kinetic energy of the incident ions is deposited into electronic ionization. At low ion velocity (ion energy  $< 10$  keV), the energy loss is dominated by nuclear collisions. This leads to a defect structure in the target, that reduces the atomic order and eventually even leads to total amorphization and to a reduced atomic density.

Figure 1 shows the calculated energy deposition per  $\text{He}^+$  ion into electronic excitation,  $(dE/dz)_{el}$ , and nuclear collisions,  $(dE/dz)_n$  for 2 MeV  $\text{He}^+$  implantation into  $\text{KNbO}_3$ . The maximum nuclear recoil energy

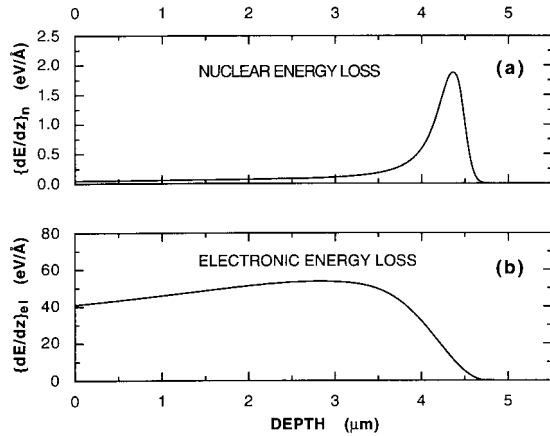


Fig. 1. Energy loss of 2 MeV  $\text{He}^+$  ions in  $\text{KNbO}_3$  due to (a) nuclear collisions and (b) electronic excitation as a function of the penetration depth calculated with the TRIM'89 code.

transfer is  $1.9 \text{ eV}/\text{\AA}$  per incident ion in a narrow layer at a depth of  $4.4 \mu\text{m}$  below the crystal surface. The maximum energy loss due to electronic excitation is  $54 \text{ eV}/\text{\AA}$  and occurs at a depth of  $2.8 \mu\text{m}$ . Even though the energy loss from the nuclear interactions at its peak is about 30 times smaller than the loss from electronic interactions, essentially only the nuclear collisions define the refractive index profile. This can be seen from the location of the peak and the shape of the curve in Fig. 1, which coincides quite well with the barrier of the optical index profile as shown in Fig. 3 [7–10].

One of the advantages of ion implantation is the relative ease to vary the thickness by changing the ion energy. Figure 2 shows the depth  $d_n$  of the nuclear

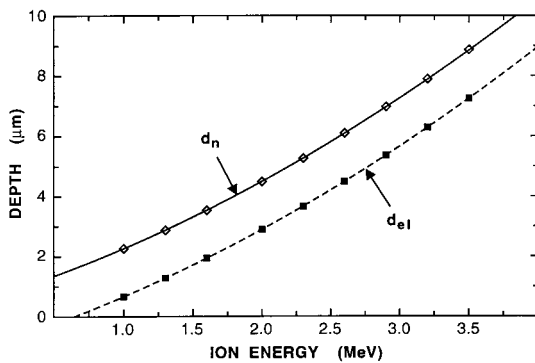


Fig. 2. Depth position of the electronic energy loss maximum (■) and the nuclear damage peak (◆) in ion-implanted  $\text{KNbO}_3$  as a function of the  $\text{He}^+$  ion energy.

collision damage peak (ion penetration range) together with the position of maximum electronic energy loss  $D_{el}$  as a function of the ion energy. The depth profile of the optical index is very close to the nuclear damage profile for MeV  $\text{He}^+$  ion implantation. One observes an optical barrier which confines a guiding region of practically unchanged index (see Fig. 3). The detailed profile may be somewhat more complex. First, the profile of retained lattice damage may not correspond directly to the nuclear energy deposition profile. This is because point defects in the nuclear damage tail may be annealed during implantation; or, conversely, defect production may be increased in the nuclear tail region by synergistic effects due to the electronic stopping energy. In addition, high dose saturation effects may lead to “flat top” barrier index profiles. Second the refractive index change depends on the volume expansion ( $\Delta V$ ) due to lattice damage, but also on the change of the atomic bond polarizability ( $\Delta\alpha$ ) and, for heavy lattice damage, on a change of the structure factor ( $\Delta\kappa$ ).

The Clausius-Mosotti equation describes, how the refractive index  $n$  depends on the polarizability  $\alpha$  and the atomic density  $N$ :

$$\frac{n^2 - 1}{n^2 + 2} = (1 + \kappa) \frac{N\alpha}{3\epsilon_0}$$

$\epsilon_0$  is the dielectric permittivity, and  $\kappa$  is introduced to account for structural effects in crystalline materials [11].  $\kappa$  vanishes in an amorphous solid or a cubic crystal and is positive in a crystal as  $\text{LiNbO}_3$  or  $\text{KNbO}_3$ . Differentiation leads to

$$\frac{\Delta n}{n} = \frac{(n^2 - 1)(n^2 + 2)}{6n^2} \left( -\frac{\Delta V}{V} + \frac{\Delta\alpha}{\alpha} + \frac{\Delta\kappa}{1 + \kappa} \right)$$

It will be shown that for a low implantation dose, which provides low-loss waveguides, the change of the polarizability ( $\Delta\alpha$ ) is the dominant effect to alter the refractive indices in  $\text{KNbO}_3$ .

A series of planar waveguides have been fabricated with 2 MeV  $\text{He}^+$  ion implantation by successively increasing the dose. The waveguide mode indices were measured at a wavelength of 632.8 nm with the prism coupling technique, and an index profile reconstruction method was then used to obtain the index profile. Figure 3 shows a typical index profile as obtained by this method together with the measured waveguide mode indices.

Figure 4 shows, how the increase of the implanta-

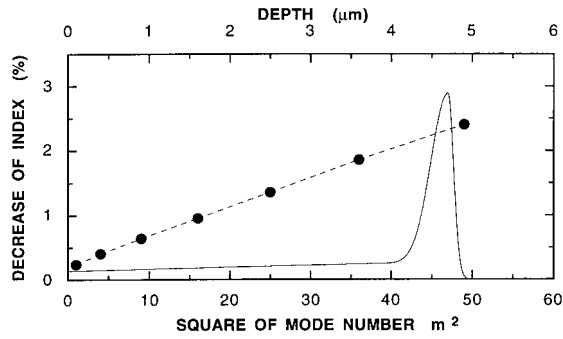


Fig. 3. Effective mode indices (●) and the reconstructed index profile for  $n_b$  (solid curve) plotted as a percentage decrease in the refractive index versus the square of the mode number (lower scale) and the depth (upper scale), respectively. The dashed curve connects the calculated mode indices measured at a wavelength of 632.8 nm.

tion dose changes the refractive indices in the barrier region. The data demonstrate the “saturation” of the index change at a dose of  $10^{16}$  ions/cm<sup>2</sup>. At that dose, the material in the barrier region has completely lost its (ferroelectric) crystalline anisotropy. The three indices  $n_a$ ,  $n_b$  and  $n_c$  have merged to one value.

In order to analyze the implantation effects, it is useful to calculate the energy deposited into nuclear collisions and to correlate the deposited energy to lattice disorder and volume changes. Irmscher et al. have implanted KNbO<sub>3</sub> crystals with He ions at 200 keV and measured the resulting disorder by RBS/channeling [12]. Fluck has performed volume expansion measurements [13]. The results are shown in Fig. 5 and summarized as follows.

There are three distinct regions of damage [13]:

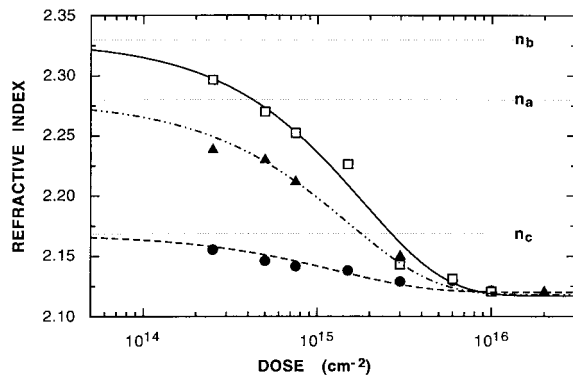


Fig. 4. Refractive indices  $n_a$  (▲),  $n_b$  (□), and  $n_c$  (■) in the barrier (region of maximum damage) as a function of the dose for 2 MeV He<sup>+</sup> ion implantation into KNbO<sub>3</sub>.

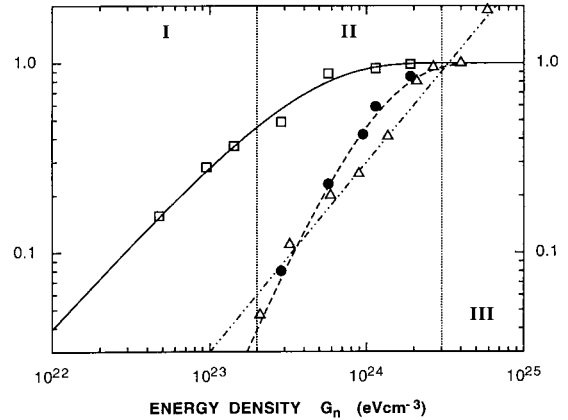


Fig. 5. Relative change of the refractive index  $n_b$  (□), lattice damage (●) and volume expansion (◇) as a function of the energy  $G_n$  deposited by nuclear collisions for He<sup>+</sup> ion implantation into KNbO<sub>3</sub>. The change is normalized to unity at saturation for the index and is given in percent of channeling yield for the lattice damage and in percent of volume change, respectively.

1. *Pre-damage stage* ( $G_n < 2 \cdot 10^{23}$  eVcm<sup>-3</sup>): the damage is characterized by point defects mainly caused by the shift of atoms from their regular lattice sites in the target material. No volume expansion is observable, but a decrease of the refractive indices of order 50% of the maximum change without significant variation of the birefringence is seen. Because lattice damage and volume expansion are negligible, the change of the refractive indices is mainly caused by a decrease of the electronic polarizability. In fact, this decrease of the polarizability due to irradiation can be directly observed by measuring the nonlinear optical susceptibility. For example, by 2.6 MeV He<sup>+</sup> ion irradiation with a dose of  $7.5 \cdot 10^{14}$  cm<sup>-2</sup>, which corresponds to an energy deposition of  $1.2 \cdot 10^{23}$  eVcm<sup>-3</sup> into nuclear collisions, the nonlinear optical susceptibility, and hence the polarizability, is reduced to about 55%.
2. *Heavy damage stage* ( $2 \cdot 10^{23}$  eVcm<sup>-3</sup> <  $G_n$  <  $3 \cdot 10^{24}$  eVcm<sup>-3</sup>): in this region the damage is characterized by the formation of clusters of point defects which provide partial amorphization of the crystalline material. This is connected with a further decrease of the refractive indices up to the maximum change. The volume dilatation caused by the amorphization gives the main contribution to the change of the refractive indices due to the decrease of the density.

3. *Saturation stage* ( $3 \cdot 10^{24} \text{ eVcm}^{-3} < G^n$ ): the lattice damage as well as the change of the refractive indices saturate in this range, indicating a total amorphization of the crystalline  $\text{KNbO}_3$ . A comparison between  $\text{KNbO}_3$  and  $\text{LiNbO}_3$  shows that the refractive indices of  $\text{KNbO}_3$  are about 20 times more sensitive to radiation damage, whereas the crystal lattice of  $\text{KNbO}_3$  is only about 2.5 times more sensitive.

## 2.2. Planar and Channel Waveguides

For the fabrication of planar waveguides, as shown in Fig. 6, the implantation has to be laterally homogeneous. In our experiments, the ion beam was scanned over an area of about  $2 \cdot 2 \text{ cm}^2$  to ensure homogeneity. The incidence of the ions was along the  $c$ - or  $b$ -axis and was slightly off normal to avoid channeling effects. The ion beam was defocused to a spot size of about  $1 \text{ cm}^2$ . The crystals were well heat sunk and the ion flux was kept at about  $2 \cdot 10^{15} \text{ cm}^{-2} \text{ h}^{-1}$  to prevent heating and charge build-up in the samples that might lead to depoling of the single domain  $\text{KNbO}_3$  crystals.

Homogeneous irradiation of  $\text{KNbO}_3$  crystals produces an index barrier at a depth of a few microns which separates a planar waveguide from the substrate material. Ion-implanted planar waveguides are quite important because they allow to perform prism-coupling and optical mode index analysis for reconstructing the refractive index depth profiles [14–16].

For most integrated optical applications channel waveguides are more desirable than planar guides, because they offer compatibility with fibres, confine-

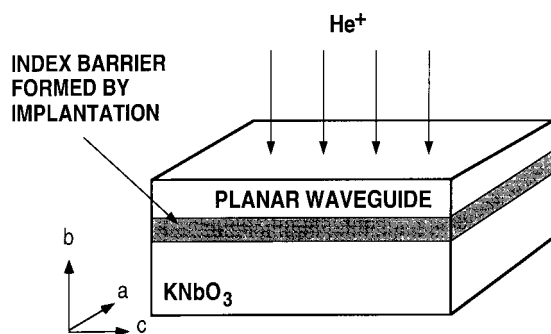


Fig. 6. Formation of a planar waveguide in  $\text{KNbO}_3$  by MeV  $\text{He}^+$  ion implantation along the crystallographic  $b$ -axis.

ment of the guided light in both lateral directions, and a higher light intensity, which leads to strong nonlinear optical interactions. They also permit easy end-fire coupling with standard microscope objectives or spherical lenses.

$\text{He}^+$  ion implantation into  $\text{KNbO}_3$  causes a decrease of the refractive index and can therefore be used to form the boundaries of optical channel waveguides. By shielding a suitable area of the  $\text{KNbO}_3$  planar waveguide with a mask from further ion irradiation, regions of reduced refractive index can be formed around a region of substantially undamaged material, which forms the channel guides. We have demonstrated the formation of permanent channel waveguides in  $\text{KNbO}_3$  and their performance for blue light second-harmonic generation [17,18].

Corresponding to the depth of the waveguides, MeV  $\text{He}^+$  ion implantation calls for a few microns thick masks to efficiently stop the incident ions. For example, the required thickness of a gold mask for completely shielding 2 MeV  $\text{He}^+$  ions is at least  $3 \mu\text{m}$ . In another approach, a set of tungsten wires ( $5 \mu\text{m}\phi$  to  $13 \mu\text{m}\phi$ ) was used to completely shield stripes of the planar waveguide from further  $\text{He}^+$  ion irradiation, and hence from further refractive index modification (Fig. 7). A more sophisticated approach with lithography, lift-off, and additional electroplating was used to fabricate ion-implanted channel waveguides in  $\text{LiNbO}_3$  [19,20].

The vertical side walls of the channels may be formed with  $\text{He}^+$  ion implantation under varying incident angle. Use of an oblique angle of incidence for the ions has the effect of reducing the depth

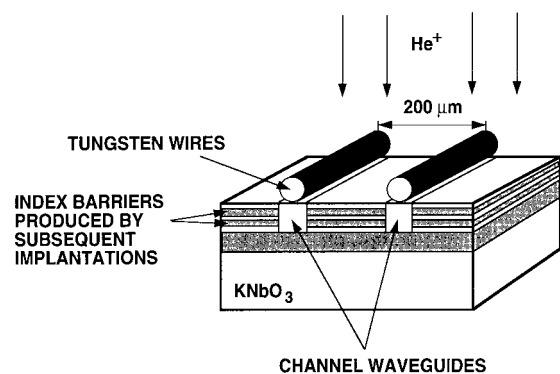


Fig. 7. Formation of optical waveguides by  $\text{He}^+$  ion implantation using a shielding mask consisting of a set of tungsten wires with a diameter of a few microns.

position of the damage barrier from the sample surface. The plane of incidence of the ion beam was along the direction of the tungsten wires. Ideally, the implantation mask would possess vertical walls and uniform thickness. But because of using wires, there are ions which pass through the outer thinner part of the wires, therefore reducing the effective width of the channel waveguides. Because these ions lose part of their energy before reaching the crystal surface they penetrate less deeply into the crystal, hence the side wall damage layers will continuously rise to the surface, reducing the waveguide width especially near the surface. The lateral straggling of the incident ions which is due to the interaction with the target ions leads also to a narrowing of the width of the strip guides [19]. As a result, the actual width of the strip waveguides formed by using tungsten wires of  $13\ \mu\text{m}$  in diameter was found to be equivalent to an implantation mask of  $\sim 11.4\ \mu\text{m}$ .

The formation of vertical side walls as shown in Fig. 7 can also be achieved with a succession of lower-energy  $\text{He}^+$  ion implants [17,18]. These additional implantation steps at lower ion energy produce similar index modifications as the planar implant but the barriers of maximum index change are located closer to the surface due to the lower energy of the ions. In the low-dose regime, the total modification of the index is given by the sum of the index changes induced by the single implantation steps. Hence, the refractive index of the unshielded region of the sample is not only decreased at the depth of the planar first implantation but also in the near-surface region (see Fig. 8a). As a result, symmetric side walls of the channel waveguides are formed with a minimum index change of  $\Delta n \approx -0.01$  (see Fig. 8b).

Figure 9 shows a picture of the endface of an ion-implanted  $\text{KNbO}_3$  channel waveguide [13]. The implantation induced barriers of strong refractive index change can be clearly seen as dark stripes whereas the almost undamaged regions between the barriers, the region of the channel waveguide and the bulk crystal are bright. This photograph demonstrates that multi-energy implantation produces channel waveguides with a nearly rectangular shaped cross section. The side walls are slightly inclined with respect to the crystal surface, because the direction of incidence of the ions which was about 10 degrees off normal.

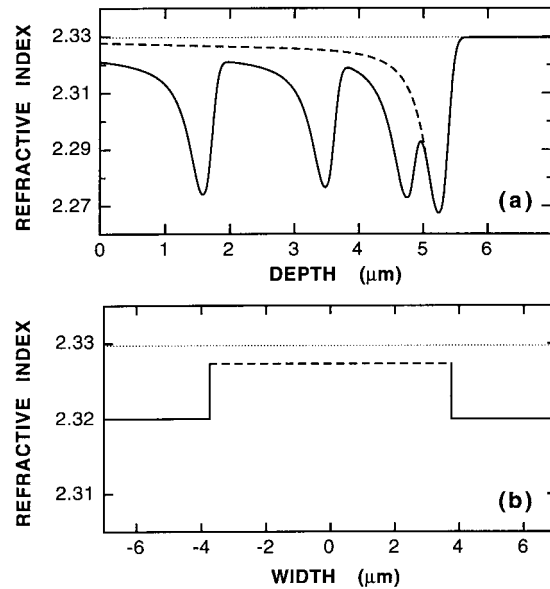


Fig. 8. (a) Refractive index profile in the shielded (---) and unshielded (—) region of a  $\text{KNbO}_3$  channel waveguide after the multiple-energy implantations. The multiple-barrier profile shows a minimum index change of  $\Delta n = -0.01$  in the side walls of the channels. (b) Resulting step-like index profile of the channel waveguide in the direction parallel to the surface at a depth of  $0.3\ \mu\text{m}$ .

### 2.3. Waveguide Losses

Losses in ion-implanted waveguides originate from three contributions: scattering, absorption, and tunneling [21]. Scattering may occur either in the bulk of the waveguide or at the waveguide surface. Surface scattering is the loss due to the interaction of the optical wave with the interface between the waveguide and its surrounding region. Its amount is determined by the roughness of the interface. Volume scattering is caused by material inhomogeneities. Such imperfections can originate from local index fluctuations, contaminant atoms, and defects within the waveguide. A small number of point defects formed during the irradiation process are found in the bulk of the waveguiding layer. However, the density of defects is highest in the barrier region at the end of the ion track. We consider the scattering at the waveguide-barrier interface as volume scattering. This is justified because this boundary is not as sharp as the waveguide-cladding interface in a thin-film waveguide, and, moreover, it is not possible to distinguish between scattering occurring in the bulk

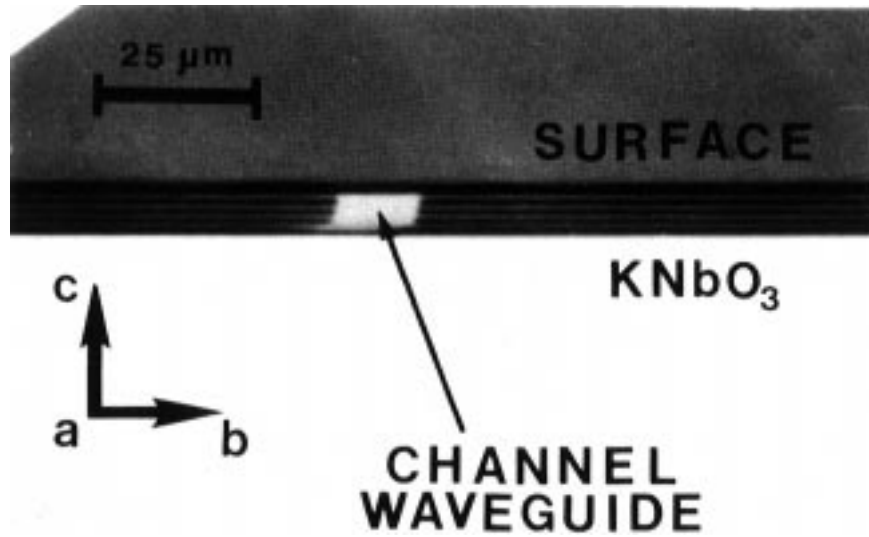


Fig. 9. Microscope picture of the cross section of an ion-implanted  $\text{KNbO}_3$  channel waveguide obtained in transmission with crossed polarizers and a magnification of  $500\times$ . The boundary of the channel guides towards the bulk crystal was produced with a single-energy  $\text{He}^+$  implantation whereas the side walls were formed by multiple-energy  $\text{He}^+$  implants (triple of dark stripes parallel to the crystal surface).

of the waveguiding layer and at the barrier interface. Thus surface scattering denotes scattering at the air-waveguide interface only [21].

Absorption in crystalline ferroelectric materials is due to contaminant atoms or vacancies present in the crystal lattice. This intrinsic material absorption turns out to be very small compared to the other contributions. However, in ion-implanted waveguides additional absorption loss can arise from defects, which may be reduced by annealing [22,23].

Leakage or tunneling of light out of the waveguide into the bulk of the crystal is an inherent property of barrier waveguides in which the optical confinement is provided by a layer of decreased refractive index of finite width. Tunneling can be minimized by proper shaping of the barrier, e.g., by increasing the

refractive-index change in the barrier through a high irradiation dose or by widening the barrier by a multiple-energy implantation process.

The main losses stem from volume scattering and absorption by defect centers and from tunneling, i.e., mechanisms correlated to the implantation process. Therefore minimizing the attenuation is essentially a matter of finding the best implantation parameters.

Experimentally, intrinsic material absorption, surface scattering, and tunneling can easily be separated from the other contributions. However, it is not possible to distinguish between absorption and scattering by defect centers induced by irradiation. Hence we use the term irradiation-induced absorption to denote the sum of both these contributions.

As it is shown in Table 1, each mechanism has

Table 1. Main loss mechanism in ion-implanted waveguides and their trend with respect to wavelength, dose and guide cross-section [from Ref. 21]

Mechanism	Cause	Trend with increasing wavelength $\lambda$	Trend with increasing ion dose $D$	Trend with increasing waveguide thickness $d$
Tunneling	Leakage of light through index barrier	Increase $\sim \lambda^7$	Decrease $\sim D^{-2}$	Decrease $\sim d^{-4}$
Implantation-induced absorption	Point defects in guiding layer and index barrier	Decrease $\sim \lambda^{-3}$	Increase $\sim D^3$	Decrease $\sim d^{-2}$
Material absorption	Impurities, contaminant atoms	Decrease $\sim \lambda^{-4}$	Constant	Constant
Surface Scattering	Roughness of air-waveguide interface	Constant	Constant	Decrease $\sim d^{-3}$

different characteristics, which makes it a difficult task to optimize a waveguide for a given application. For example, losses of 2 dB/cm at the fundamental and the second-harmonic wavelength reduce the conversion efficiency by more than a factor of 2, if a waveguide of 1 cm length is used [21].

It is very instructive to study the Figs. 10 and 11, because they demonstrate, that the minimum attenuation cannot be achieved for both wavelengths of a SHG (second harmonic generation, frequency doubling) configuration simultaneously. Figure 10 shows, that the fundamental wavelength (0.870  $\mu\text{m}$ ) needs an implant dose of  $3 \cdot 10^{15} \text{ cm}^{-2}$  to minimize tunneling, while the blue light at 0.45  $\mu\text{m}$  is already noticeably

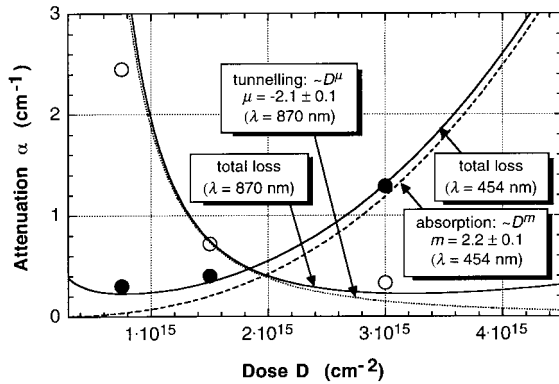


Fig. 10. Attenuation as a function of ion dose at 0.454 and 0.870  $\mu\text{m}$  of planar waveguides of 4.5  $\mu\text{m}$  thickness. Solid curve: total loss; dashed curve: absorption loss at 0.454  $\mu\text{m}$ ; dotted curve: tunneling loss at 0.870  $\mu\text{m}$ ; circles: measured attenuation [21].

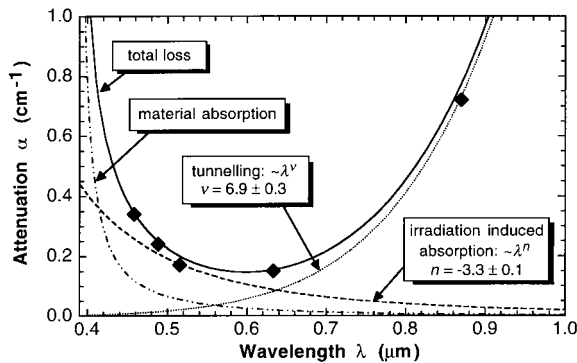


Fig. 11. Attenuation as a function of wavelength of a planar waveguide of 4.5  $\mu\text{m}$  thickness formed with an ion dose of  $1.5 \cdot 10^{15} \text{ cm}^{-2}$ . Solid curve: calculated total loss; dashed curve: irradiation-induced absorption; dotted curve: tunneling; dotted-dashed curve: material absorption; diamonds: measured attenuation [21].

absorbed at this dose and calls for a lower implantation dose [21].

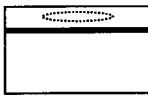

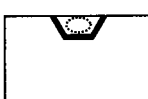
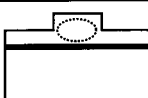
Independent on the waveguide type, the attenuation follows identical trends with respect to wavelength, ion dose, guide thickness, and guide width. However, the values of the attenuation coefficient vary considerably. Figure 12 compares the loss of different waveguides at the wavelengths of 0.515  $\mu\text{m}$  and 0.870  $\mu\text{m}$ , respectively. The waveguide fabrication parameters are the following: ion dose  $D = 1.5 \cdot 10^{15} \text{ cm}^{-2}$ , guide thickness  $d = 5.3 \mu\text{m}$ , and guide width  $w = 5 \mu\text{m}$  for the channel guides. These are typical parameters used to fabricate waveguides for second-harmonic generation (SHG) [24]. By using a specially processed thick photoresist, the embedded barrier guide (Fig. 12) can be fabricated with one implantation step only [25].

Clearly, the lowest attenuation is measured in planar waveguides, as there is no interaction of the optical field with the lateral guide-surround interface. For channel waveguides the lowest attenuation is measured in ridge waveguides. The need of one implantation step only, the precise patterning of the mask, and the sputtering process, affecting the material only at the surface, permit to produce waveguides of high quality with low loss.

In embedded channel waveguides the lateral confinement formed by a multiple-energy implantation process causes an increase of absorption loss. In addition, the side walls of the channel are inherently irregular leading to an increase of the scattering loss. This explains the higher loss of these waveguides. In embedded barrier waveguides both lateral and bottom confinement is provided by a barrier of finite width. The leakage of light through the side barriers strongly increases the attenuation at long wavelength. At short wavelengths the absorption is strong because of the interaction of the optical field with the side and bottom barriers.

The key parameter to obtain optimum performance is the ion dose. The fact that absorption and tunneling follow opposite trends with respect to ion dose is a drawback for the fabrication of waveguides for blue light second-harmonic generation. Minimizing the loss at the fundamental wave requires a high ion dose, whereas a low loss at the second-harmonic wave is obtained with a low dose. Therefore optimizing the waveguide for second-harmonic generation is a tradeoff between low and high ion doses. Intermediate doses between  $1.5$  and  $2.5 \cdot 10^{15} \text{ cm}^{-2}$



waveguide type		loss at 515 nm (cm <sup>-1</sup> )	loss at 870 nm (cm <sup>-1</sup> )
planar		0.2	0.4
embedded channel		1.2	1.4
embedded barrier		2.0*	2.3*
ridged channel <sup>+</sup>		0.8	0.6

\* calculated from measurement in a waveguide with  $d = 4.5 \mu\text{m}$  and  $w = 8 \mu\text{m}$ .  
<sup>+</sup> ridge height  $h = 0.91 \mu\text{m}$ .

Fig. 12. Comparison of the waveguide attenuation at the wavelengths of  $0.515 \mu\text{m}$  and  $0.870 \mu\text{m}$ , respectively, in different waveguides. Waveguide parameters:  $d = 5.3 \mu\text{m}$ ,  $w = 5 \mu\text{m}$  (channel waveguides),  $D = 1.5 \cdot 10^{15} \text{ cm}^{-2}$  [24].

are considered to be the most suitable for second-harmonic generation.

The preceding discussion concentrated on the implant ion He (mass 4). Very similar results can be achieved with H (mass 1). In the case of H, the attainable depth is larger by a factor of approx. 4 at identical accelerator energy [26].

### 3. Improvement of Photorefractive Properties

Several of the optical ferroelectrics show photorefractive properties, for instance  $\text{KNbO}_3$ ,  $\text{BaTiO}_3$ ,  $\text{LiNbO}_3$  and  $\text{Sr}_{1-x}\text{Ba}_x\text{Nb}_2\text{O}_6$  (SBN). Typically melt doping with transition metal ions has been investigated to modify the photorefractive (PR) response. The PR effect is best understood in a band structure picture (Fig. 13) with donors, traps and an inhomogeneous illumination: mobile carriers (electrons or holes) are created by photon absorption (Fig. 14) [27]. They diffuse into dark zones and a charge pattern builds up, which in turn creates an electrical field pattern (Fig. 15). In an electrooptical ferroelectric this causes an index pattern, which can be observed in diffraction or optical beam mixing experiments. Applications of the effect are envisioned in the field

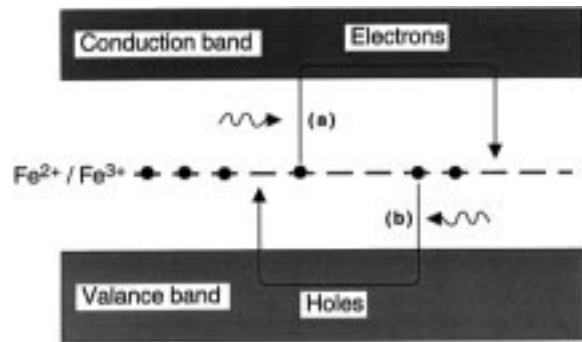


Fig. 13. Band scheme for Fe-doped  $\text{KNbO}_3$  with two types of charge carriers and one trap center (Fe) with two different valence states ( $\text{Fe}^{3+}$  and  $\text{Fe}^{2+}$ ). The position of the levels represents the ionization energy. The photoexcitation of (a) electrons and (b) holes is shown.

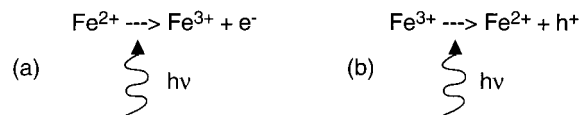


Fig. 14. Charge transfer processes, leading to the creation of (a) electrons and (b) holes in Fe-doped  $\text{KNbO}_3$ .

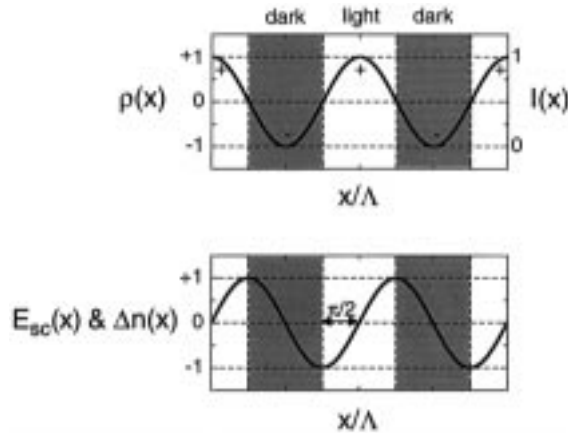


Fig. 15. Schematic view of the formation of charge  $\rho(x)$  and electric-field gratings  $E_{sc}(x)$  through diffusion during illumination and resulting refractive index modulation  $\Delta n(x)$ .  $\Delta$  is the grating wave vector. Diffusion provides a phaseshift of  $90^\circ$  between the original interference grating and the resulting refractive index grating.

of switching and in holographic memories. It is a new and important discovery, that the ion beam generated oxygen defects modify the photorefractive properties in a very controlled way, see Fig. 16. This has been described in detail in [27–29]. The authors demonstrate the controlled and reproducible adjustment of the photorefractive properties such as gain and response time in Fe-doped KNbO<sub>3</sub> by using MeV proton-irradiation. The observations are explained by a change in the reduction ratio  $R = [\text{Fe}^{2+}]/[\text{Fe}^{3+}]$  in the irradiated region due to the production of oxygen vacancies during proton-irradiation. The reduction

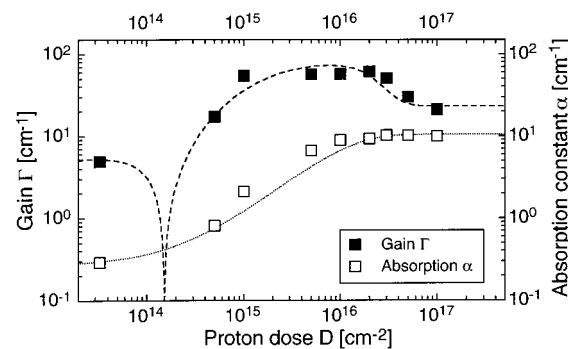


Fig. 16. Exponential gain  $\Gamma$  and absorption constant  $\alpha$  for a Fe-doped KNbO<sub>3</sub> crystal as a function of the proton irradiation dose  $D$ . The curves represent the theoretical model [27]. The steep drop at a dose of  $1.5 \cdot 10^{14}$ /cm<sup>2</sup> is due to a change of the sign of the majority carriers from holes to electrons.

ratio  $R$  can be precisely adjusted over a very large range from  $R=0.01$  up to  $R=40$ , unmatched by former methods, by choosing the appropriate irradiation dose. The photorefractive gain  $\Gamma$  is improved from  $2.5 \text{ cm}^{-1}$  up to  $34 \text{ cm}^{-1}$ , the absorption constant  $\alpha$  from  $0.06 \text{ cm}^{-1}$  up to  $2.1 \text{ cm}^{-1}$  and the grating buildup time  $\tau$  from  $1.6 \text{ ms}$  to  $34 \mu\text{s}$  at an intensity  $I=200 \text{ W/cm}^2$  (corresponding to a power of  $2.5 \text{ mW}$  in the interaction region) in a 1000 ppm Fe-doped KNbO<sub>3</sub> crystal, for example.

These experiments were performed at  $\lambda=514.5 \text{ nm}$ . Moreover, ion implantation permits the extension of the photorefractive response from the visible into the near-infrared telecommunication wavelength regime of  $1.3$  and  $1.5 \mu\text{m}$ . This is shown in Fig. 17 and has not been observed in any other ferroelectric material before [28].

#### 4. Ion Implantation Doping and Solid Phase Epitaxy

LiNbO<sub>3</sub> is the most commonly used electrooptical crystal [30]. Its main optical application field are modulators. The crystalline structure is of the ilmenite type. Optical waveguides in LiNbO<sub>3</sub> can be created by depositing lithographically patterned Ti stripes of a few tens of nm thickness and a width of some

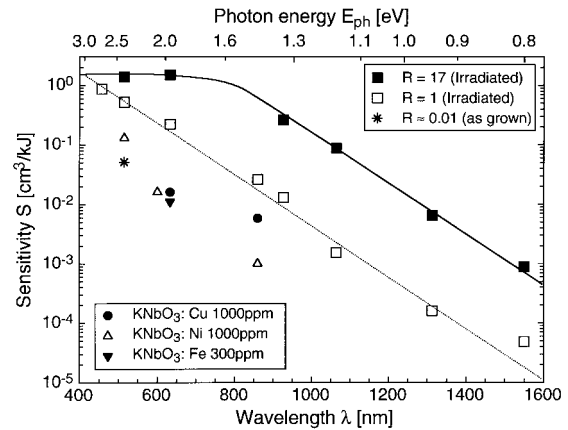


Fig. 17. Comparison of the photorefractive sensitivity  $S$  as a function of wavelength for different KNbO<sub>3</sub> crystals. (\*): KNbO<sub>3</sub>, as grown, melt doped with 1000 ppm Fe (□): identical crystal, irradiated with protons to achieve a reduction ratio  $R=1$  (■): identical crystal, irradiated with protons more strongly, to a reduction ratio  $R=17$ . The other crystals are not irradiated and melt doped as denoted in the graph. The irradiated crystals always show the best sensitivity [27].

micrometers on the surface of the wafer and diffusing the Ti into the crystal, typically at 1000°C [30]. Inside the crystal, the Ti is incorporated into positions resulting in the formation of  $\text{TiO}_6$  octahedra, which have a higher polarizability than the matrix, in particular the  $\text{NbO}_6$  octahedra [31]. By this process, the ordinary and the extraordinary indices are raised, and a stable waveguide is formed. Noticeably higher local Ti concentrations and much steeper Ti concentration gradients can be achieved by implanting Ti into  $\text{LiNbO}_3$  and many waveguide devices have made use of this technology [32]. During implantation, the  $\text{LiNbO}_3$  crystallinity is damaged and an annealing step is needed, typically at 1000°C, but during the regrowth of the crystalline, heavily Ti-doped material, more Ti is incorporated into the bulk than would be possible by Ti in-diffusion. Waveguides with up to 18 mol% (3.6 at%) of Ti in  $\text{LiNbO}_3$  of optical quality have been fabricated [33–35]. This Ti dose produces an increase of 0.040 of the index  $n_c$  and 0.019 of the index  $n_o$ , compared with the bulk values of  $n_c = 2.20$  and  $n_o = 2.28$ . At these high dopant concentrations, the regrowth is a complex process that involves the diffusion of all constituents plus additional oxygen, normally supplied from the oven atmosphere. At lower dopant concentrations (< 0.1 at%) the situation becomes more simple, and Poker has demonstrated how the crystallization starts at the amorphous/crystalline interface and proceeds towards the surface. This recrystallization can be described as solid phase epitaxy (SPE), and the SPE is characterized by the low activation energy of 2 eV. As a consequence, these experiments could be performed in the fairly low temperature range of 400 to 500°C [36].

From these experiments it has become obvious that the ilmenite structure of  $\text{LiNbO}_3$  with its high concentration of structural vacancies and its relatively mobile Li ions may be fairly easily doped by ion implantation. The restoration of short-range order is possible, as seen in the Er PL signal [37], as well as the complete restoration of long-range order with the desired electro-optical properties. This has been established by RBS/channeling experiments, which prove the lattice perfection, as well as by the construction of electro-optical devices, which show the perfect performance of the material. In contrast, the densely packed perovskites as  $\text{KNbO}_3$  or  $\text{BaTiO}_3$  do not show the same amount of tolerance if implantation of heavy ions at higher doses is performed, and the completion of SPE may be much

more difficult or even impossible. This is especially true if different crystallographic phases are encountered during the annealing procedure, or if the necessary annealing temperatures result in the loss of one component into the oven atmosphere (or vacuum) [38].

The introduction of laser/amplifier-active ions as Er into  $\text{LiNbO}_3$  offers attractive possibilities for new devices.  $\text{LiNbO}_3$  is commercially available in the form of undoped wafers. The possibility to dope these wafers with Er by ion implantation has been demonstrated, and the diffusion data have been established [39,40]. In the meantime, Er-diffused  $\text{LiNbO}_3$  waveguide lasers have been constructed. MeV ion implantation offers the additional possibility to administer the Er doping into a certain depth into the crystal. This is done because it is advantageous to bring the dopant into the central area of an optical waveguide, where the pumping and signal field strengths are at their maximum.

Analogous to the observed behavior of Er implanted in glass, the implanted Er in  $\text{LiNbO}_3$  also needs some thermal annealing in order to establish its characteristic photoluminescence (PL). It is surprising that the full Er PL signal is already observed after a short anneal of 1 min at the low temperature of 500°C [37]. This proves that the  $\text{Er}^{3+}$  ion has configured itself into an appropriate oxygen environment long before the  $\text{LiNbO}_3$  host crystal is able to restore long-range order and its lattice perfection.

A “slow” annealing procedure of the Er implanted samples in a tube furnace causes the recrystallization of the amorphized surface layer by columnar solid-phase epitaxial regrowth (SPE). The resulting grain boundaries do not influence the photoluminescence (PL) of the Er ions but the low crystal quality of the surface layer is unfavorable for waveguiding operation. Annealing for 8 h at 1060°C is necessary to remove all grain boundaries, leading to significant diffusion broadening of the Er profile. The columnar SPE regrowth can be avoided completely by rapidly heating the implanted  $\text{LiNbO}_3$  samples to the final annealing temperature [41]. Using a rapid thermal annealer (RTA) at a heating rate of about 100°C/s, no columns are formed, and an amazingly short annealing time of 1 min at 1060°C is sufficient to cause perfect epitaxial recrystallization. Using this procedure, a concentration of up to 0.18 at% optically active Er ions can be incorporated into the  $\text{LiNbO}_3$  lattice. One possible explanation is that at high

temperatures (where the crystallization takes place after rapid heating), the formation of defects disturbing the planar growth front is slow relative to the SPE growth rate, whereas at lower temperatures stable non-epitaxial crystallites may nucleate in the amorphous phase and obstruct the proceeding epitaxial growth front. Such defects result in low quality recrystallization.

Figure 18 shows the Er depth profiles of three LiNbO<sub>3</sub> samples implanted with  $5 \cdot 10^{15}$  Er/cm<sup>2</sup> at 3.5 MeV [41]. The as-implanted profile is nearly Gaussian shaped, and peaks at a depth of 0.78  $\mu$ m. The peak concentration is 0.11 at%. Annealing the sample for 8 h at 1060°C in a tube furnace causes a significant widening of the Er depth profile. Er ions have diffused into the bulk and towards the surface. In contrast, the sample annealed for 1 min at 1060°C using the RTA (rapid thermal anneal) shows a much sharper profile. The surface concentration has increased as compared to the as-implanted profile, but no Er diffusion into the bulk is observed. The different shape of the two Er depth profiles is a result of the different annealing times: using the very short annealing time in the RTA, the Er diffusion into the bulk can be avoided and only defect enhanced diffusion of Er ions towards the surface during the recrystallization of the amorphous phase remains. Gain calculations for a waveguide amplifier based on a proton-exchanged waveguide predict a reduction of the threshold pump power by a factor of 2 for the narrower Er profile as compared to the profile of a tube furnace annealed sample due to the improved matching to the optical mode.

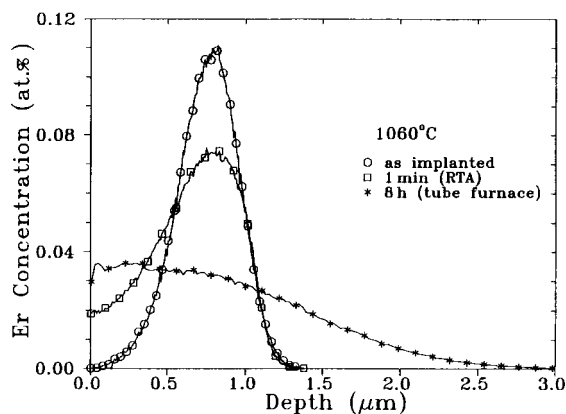


Fig. 18. SIMS depth profiles of Er implanted (3.5 MeV,  $5 \cdot 10^{15}$  Er/cm<sup>2</sup>) LiNbO<sub>3</sub> single crystals, annealed at 1060°C in the tube furnace (8 h) or the RTA (1 min, warm-up rate 100°C/s).

## 5. Direct Growth of Thin Ferroelectric Optical Films

In the first 4 chapters ion implantation into ferroelectrics has been discussed. This process is always limited to the near-surface region due to the limited penetration depth of the ions. One could try to grow thin films with the desired optical properties, since all functions of integrated optics are limited to the near-surface regime anyway.

In fact, there is a huge body of literature on ferroelectric thin films, which may be useful for optical applications [42–44]. Unfortunately, very few films have been used for waveguiding and no thin film device has been presented so far. Instead, the epitaxial growth of low loss ferroelectric thin films has been frustratingly difficult. Fork et al. had estimated the magnitude of the different loss contributions within the waveguides [43]. They came to the conclusion, that especially the scattering losses from rough surfaces pose a severe obstacle. Comparing samples from many groups, they found for most films an rms surface roughness of 1% of the film thickness. Typical films for optical waveguides have to be approx. 1  $\mu$ m thick. From their loss calculations, an rms surface roughness of 1 nm would be acceptable, a factor of 10 less than actually achieved for these films. They suspected a somewhat hopeless situation.

Nevertheless, many groups have worked on the growth of these films. At Jülich, we were able to use the Pulsed Laser Deposition (PLD) to grow very smooth films of BaTiO<sub>3</sub> on MgO of 1  $\mu$ m thickness and an rms surface roughness of only 1.1 nm [44,45]. This has been measured by Atomic Force Microscopy (AFM). The surface appeared very flat; only some small islands were visible. The maximum variation in height (peak-to-valley (PV) roughness) is 5.2 nm, corresponding to an rms roughness of 1.1 nm. This is only 0.1% of the deposited thickness. For samples of a smaller BaTiO<sub>3</sub> film thickness, even lower roughness values were found. The AFM measurements suggest that no prohibitive contribution to waveguide losses is expected from the surface morphology.

An optical analysis of the propagation losses in planar waveguides led to an overall loss of 2.9 dB/cm. We have recently published the growth conditions and the structural and optical characterization of these films [45]. Figure 19 shows the measured indices for various of these highly transparent BaTiO<sub>3</sub> films.

At several places the growth of BaTiO<sub>3</sub> films has

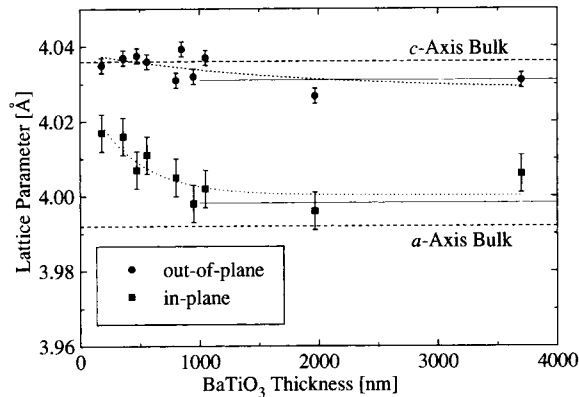


Fig. 19. In-plane and out-of-plane indices plotted for a series of BaTiO<sub>3</sub> films grown on MgO with various thicknesses. The straight line is a guide for the eye. The dotted lines indicate the BaTiO<sub>3</sub> bulk values.

been studied [43–51], but so far only two laboratories have been able to demonstrate the phase modulation of light propagating in a thin film of BaTiO<sub>3</sub>. At Oak Ridge National Laboratory, a dedicated molecular beam epitaxy (MBE) system has been designed and used to study the growth of various perovskites. BaTiO<sub>3</sub> films on MgO have been fabricated in very good quality [52,53]. A free beam from a He-Ne-laser was coupled into a planar BaTiO<sub>3</sub> film with a prism coupler. By applying an electrical field to the BaTiO<sub>3</sub>, the phase of the light was modulated to the tune of music.

### 5.1. A BaTiO<sub>3</sub> Ridge Waveguide Modulator

The first BaTiO<sub>3</sub> phase modulator in a ridge waveguide configuration (Fig. 20) has been demonstrated by researchers at Northwestern University [54,55]. They used low pressure metal-organic

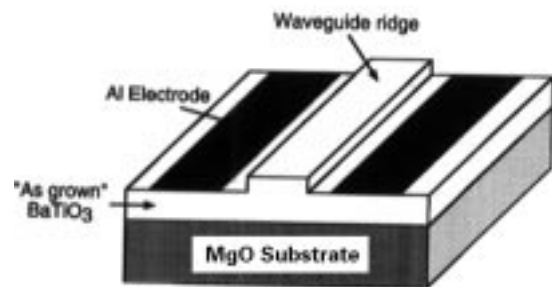


Fig. 20. Schematic representation of the ridge waveguide modulator structure [Reprinted with permission from Ref. 55. Copyright 1997 American Institute of Physics.].

chemical vapor deposition (LP-MOCVD) to grow the crystalline films of BaTiO<sub>3</sub> on MgO. After a very gentle polishing step, the ridge structure was prepared by standard lithography and wet etching. End fire coupling of a polarized beam was used to propagate the light through the waveguide. The measured phase modulation is shown in Fig. 21, which has been taken from [55]. These results are pathbreaking, because they show for the first time a thin film waveguide with sufficient transparency to establish a channel waveguide phase modulator. Their data are probably influenced by domain movement and by a small amount of ferroelectric hysteresis. They are able to estimate an effective electro-optic coefficient  $\Delta r \sim 50 \pm 5$  pm/V for their film and they could follow the frequency response of their sample up to 5 MHz. Moreover, they have used their MOCVD process to add Er into their BaTiO<sub>3</sub> waveguides [56]. At present, these waveguides are somewhat lossy. Nevertheless, stimulated emission at 1.5  $\mu$ m could be demonstrated.

### Conclusion

We conclude this review with some general remarks:

- Ion implantation has been used very successfully for damage engineering and waveguide patterning

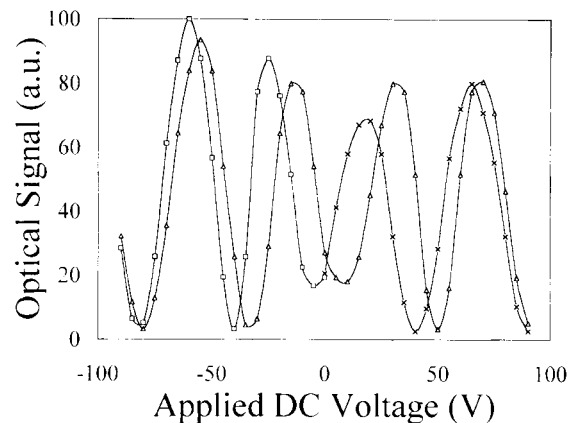


Fig. 21. Amplitude modulation in an “as-grown” thin-film BaTiO<sub>3</sub> channel waveguide vs. applied dc voltage. The data were taken as follows: a positive voltage was applied to the electrodes prior to data acquisition; then, starting at 0 V a negative potential was applied in 5 V increments up to  $-90$  V ( $\square$  data points); the potential was then increased from  $-90$  V to  $+90$  V ( $\Delta$  data points); and, finally, reduced from  $+90$  V back to zero ( $\times$  data points). [Reprinted with permission from [55]. Copyright 1997 American Institute of Physics.].

in a wide class of ferroelectric crystals. Today the best single mode waveguides in perovskites are fabricated by a combination of ion implantation and surface etching of ridges.

- The use of damage engineering for photorefractive doping by the introduction of oxygen vacancies is a new field. It seems especially useful, if near-infrared sensitivity is desired.
- Direct implantation doping of LiNbO<sub>3</sub> with transition metals and rare earth ions has been established. The necessary annealing schemes are complex because of the chemically different elements involved in doped ferroelectric crystals and the growth of foreign phases has to be avoided. Rapid thermal processing has been employed with good results. For LiNbO<sub>3</sub>, the competitive technique of diffusion is successful as well.
- The growth of ferroelectric optical thin films has made impressive progress and the results are clearly surpassing previous predictions. We see the first devices being constructed from thin films and our knowledge of the field is advancing rapidly. The vast potential of thin film technology with its different deposition and growth techniques and the modification by ion implantation, diffusion and etching still needs to be developed. In addition, the fabrication of hetero- and nanostructures will offer new possibilities.

### Acknowledgments

We gratefully acknowledge the cooperation with L. Beckers, S. Brülisauer, M. Fleuster, J. Schubert, T. Pliska, W. Sohler and many other colleagues. Financial support was provided by the ESPRIT LTR-Project 31838 (SCOOP).

### References

1. J.F. Ziegler, *Ion Implantation Technology*, (North Holland, Amsterdam, 1992).
2. S. Mantl, *Mat. Sci. Rep.*, **8**, 1 (1992).
3. C.W. White, J.D. Budai, J.G. Zhu, S.P. Withrow, D.M. Hembree, D.O. Henderson, A. Ueda, Y.S. Tung, and R. Mu, *Mat. Res. Soc. Symp. Proc.*, **396**, 377 (1996).
4. P.D. Townsend, P.J. Chandler, and L. Zhang, *Optical Effects of Ion Implantation*, (Cambridge University Press, 1994).
5. P. Mazzoldi and G.W. Arnold, eds., *Ion Beam Modification of Insulators*, (Elsevier, Amsterdam, 1987).
6. J.P. Biersack and L.G. Haggmark, *Nucl. Instr. and Meth.*, **174**, 257 (1980).
7. P.D. Townsend, *Rep. Prog. Phys.*, **50**, 501 (1987).
8. P.D. Townsend, *Nucl. Instr. and Meth.*, **B46**, 18 (1990).
9. Ch. Buchal, S.P. Withrow, C.W. White, and D.B. Poker, *Ann. Rev. Mat. Sci.*, **24**, 125 (1994).
10. D. Fluck, R. Irmscher, Ch. Buchal, and P. Günter, *Ferroelectrics*, **128**, 79 (1992).
11. D.T.Y. Wei, W.W. Lee, and L.R. Bloom, *Appl. Phys. Lett.*, **25**, 329 (1974).
12. R. Irmscher, D. Fluck, Ch. Buchal, B. Stritzker, and P. Günter, *Mat. Res. Soc. Proc.*, **201**, 399 (1991).
13. D. Fluck, *Ion Implanted KNbO<sub>3</sub> Waveguides for Blue Light Second Harmonic Generation* Thesis, ETH Zürich, No. 11225, (Zürich, 1995).
14. F.P. Strohkendl, D. Fluck, and P. Günter, *Appl. Phys. Lett.*, **59**, 3354 (1991).
15. D. Fluck, B. Binder, M. Küpfer, H. Looser, Ch. Buchal, and P. Günter, *Opt. Comm.*, **90**, 304 (1992).
16. D. Fluck, D.H. Jundt, P. Günter, M. Fleuster, and Ch. Buchal, *J. Appl. Phys.*, **74**, 6023 (1993).
17. D. Fluck, P. Günter, M. Fleuster, and Ch. Buchal, *J. Appl. Phys.*, **72**, 1671 (1992).
18. D. Fluck, J. Moll, P. Günter, M. Fleuster, and Ch. Buchal, *Electron. Lett.*, **28**, 1092 (1992).
19. G.T. Reed and B.L. Weiss, *Nucl. Instr. and Meth.*, **B19/20**, 907 (1987).
20. G.T. Reed and B.L. Weiss, *Electr. Lett.*, **23**, 792 (1987).
21. T. Pliska, D. Fluck, P. Günter, L. Beckers, and Ch. Buchal, *J. Opt. Soc. Am.*, **B15**, 628 (1998).
22. T. Pliska, D.H. Jundt, D. Fluck, P. Günter, M. Fleuster, and Ch. Buchal, *Electr. Lett.*, **30**, 562 (1994).
23. T. Pliska, D.H. Jundt, D. Fluck, and P. Günter, *J. Appl. Phys.*, **77**, 6114 (1995).
24. T. Pliska, *Potassium Niobate Channel Waveguides for Blue Light Second-Harmonic Generation* Thesis, ETH Zürich No. 12222 (Zürich 1997).
25. D. Fluck, T. Pliska, P. Günter, St. Bauer, L. Beckers, and Ch. Buchal, *Appl. Phys. Lett.*, **69**, 4133 (1996).
26. P. Moretti, P. Thevenard, K. Wirl, P. Hertel, H. Hesse, E. Krätzig, and G. Godefroy, *Ferroelectrics*, **128**, 13 (1992).
27. S. Brülisauer, *Control of the Photorefractive Effect in KNbO<sub>3</sub> by Ion Implantation* Thesis, ETH Zürich No. 12625 (Zürich 1998).
28. S. Brülisauer, D. Fluck, P. Günter, L. Beckers, and Ch. Buchal, *J. Opt. Soc. Am.*, **B 13**, 2544 (1996).
29. S. Brülisauer, D. Fluck, P. Günter, L. Beckers, and Ch. Buchal, *Opt. Comm.*, **153**, 375 (1998).
30. H. Nishihara, M. Haruna, and T. Suhara, *Optical Integrated Circuits* (McGraw-Hill, New York 1989).
31. Ch. Buchal, *Structure Property Relationship in Surface-Modified Ceramics* ed. C. J. Mc Hargue et al. 389 (Kluwer Dordrecht, 1989).
32. P.R. Ashley, W.S.C. Chang, Ch. Buchal, and D.K. Thomas, *IEEE J. Lightwave Techn.*, **7**, 855 (1989).
33. T. Bremer, W. Heiland, Ch. Buchal, R. Irmscher, and B. Stritzker, *J. Appl. Phys.*, **67**, 1183 (1990).
34. Ch. Buchal, *Nucl. Instr. Meth.*, **B59/60**, 1142 (1991).

35. Ch. Buchal, *Nucl. Instr. Meth.*, **B68**, 355 (1992).
36. D.B. Poker and D.K. Thomas, *J. Mat. Res.*, **4**, 412 (1989).
37. M. Fleuster, Ch. Buchal, E. Snoeks, and A. Polman, *J. Appl. Phys.*, **75**, 173 (1994).
38. St. Bauer, *Epitaxial Growth of LiNbO<sub>3</sub> on Sapphire* Thesis (German), Jül-Bericht, Forschungszentrum Jülich No. 3056 (Jülich 1995).
39. Ch. Buchal and St. Mohr, *J. Mat. Res.*, **6**, 134 (1991).
40. I. Baumann, *Appl. Phys.*, **A64**, 33 (1997).
41. M. Fleuster, Ch. Buchal, E. Snoeks, and A. Polman, *Appl. Phys. Lett.*, **65**, 225 (1994).
42. A.M. Prokhorov, Yu S. Kuzminov, and O.A. Khachaturyan, *Ferroelectric Thin-Film Waveguides in Integrated Optics and Optoelectronics* (Cambridge International Science Publishing 1996) and references therein.
43. D.K. Fork, F. Armani-Leplingard, J.J. Kingston, and G.B. Anderson, *Mat. Res. Soc. Symp. Proc.*, **392**, 189 (1995).
44. L. Beckers, *Epitaxial Ferroelectrical Thin Optical Film* Thesis (German), Jül-Bericht Forschungszentrum Jülich No. 3554 (Jülich 1998) (includes 111 references).
45. L. Beckers, J. Schubert, W. Zander, J. Ziesmann, A. Eckau, P. Leinenbach, and Ch. Buchal, *J. Appl. Phys.*, **83**, 3305 (1998).
46. R. Nawathey, R.D. Vispute, S.M. Chaudhari, S.M. Kanetkar, and S.B. Ogale, *Solid State Comm.*, **71**, 9 (1989).
47. D.H. Kim and H.S. Kwok, *Appl. Phys. Lett.*, **67**, 1803 (1995).
48. T. Okada, Y. Nakata, H. Kaibara, and M. Maeda, *Jpn. J. Appl. Phys.*, **34**, L1536 (1995).
49. S. Tsunekawa, T. Fukuda, T. Ozaki, Y. Yoneda, and H. Terauchi, *Appl. Phys. Lett.*, **71**, 1486 (1997).
50. *Mat. Res. Soc. Bulletin 17*, 2 Feb. 1992, *Pulsed Laser Deposition*.
51. S.-H. Lee, T.W. Noh, and J.-H. Lee, *Appl. Phys. Lett.*, **68**, 472 (1996).
52. R.A. McKee, F.J. Walker, E.D. Specht, G.E. Jellison, and L.A. Boatner, *Phys. Rev. Lett.*, **72**, 2741 (1994).
53. F.J. Walker, R.A. McKee, H.-W. Yen, and D.E. Zelmon, *Appl. Phys. Lett.*, **64**, 1495 (1994).
54. D.M. Gill, B.A. Block, C.W. Conrad, B.W. Wessels, and S.T. Ho, *Appl. Phys. Lett.*, **69**, 2968 (1996).
55. D.M. Gill, C.W. Conrad, G. Ford, B.W. Wessels, and S.T. Ho, *Appl. Phys. Lett.*, **71**, 1783 (1997).
56. D.M. Gill, G.M. Ford, B.A. Block, B.W. Wessels, and S.T. Ho, *Mat. Res. Soc. Symp. Proc.*, **486**, 343 (1998).